magnetochemistry

MDPI

Article

Slow Relaxation of Magnetization and Magnetocaloric Effects in One-Dimensional Oxamato-Based Lanthanide(III) Coordination Polymers †

Jhonny W. Maciel [1], Lucas H. G. Kalinke [2], Renato Rabelo [1], Meiry E. Alvarenga [1], Felipe Terra Martins [1], Nicolás Moliner [3] and Danielle Cangussu [1,*]

[1] Instituto de Química, Universidade Federal de Goiás, 74690-900 Goiânia, GO, Brazil; jhonny_willians@ufg.br (J.W.M.); renato_rabelo@ufg.br (R.R.); meiryalvarenga@yahoo.com.br (M.E.A.); felipe@ufg.br (F.T.M.)
[2] Instituto Federal de Goiás—IFG, Campus Anápolis, 75131-457 Anápolis, GO, Brazil; lucas.kalinke@ifg.edu.br
[3] Instituto de Ciencia Molecular (ICMol), Universitat de València, 46980 Paterna, Spain; fernando.moliner@uv.es
* Correspondence: danielle_cangussu@ufg.br
† We dedicate this article to Miguel Julve and Francisco Lloret, two exceptional professors and researchers whose brilliant careers were devoted to exploring coordination chemistry and studying magnetic properties. Their passion for guiding students and nurturing colleagues around the world stands as the biggest testament to their generosity and dedication. We are deeply grateful for the priceless knowledge and wisdom they shared over more than 20 years of collaboration. In loving memory of Miguel, our dear friend and colleague, whose legacy will continue to inspire us all.

Abstract: Herein, we present the synthesis and characterization of a series of isostructural lanthanide(III) compounds with the *N*-(4-carboxyphenyl)oxamic acid (H_3pcpa) ligand of the general formula as $\{[Ln_2(Hpcpa)_3(H_2O)_5]\}_n$ [Ln = Dy(III) **1**, Ho(III) **2**, Er(III) **3**]. The structure of **3** consists of neutral zig–zag chains of Er(III) ions, with $Hpcpa^{2-}$ ligands acting as bridges in a bidentate/monodentate coordination mode with five water molecules achieving the eight-coordination around the two Er(III) ions within the repeating bis(carboxylate)-bridged dinuclear units along the chain. The magnetic and magnetocaloric properties were studied for **1**–**3**. Compound **1** presents a field-induced slow relaxation of the magnetization with a "reciprocating thermal behavior" below 5 K for H = 0.25 T, while **2** shows maxima of the magnetic entropy from 3 up to 6 K for ΔH > 2 T.

Keywords: coordination chemistry; oxamato ligand; lanthanide; magnetic properties; magnetocaloric properties

check for updates

Academic Editor: Marius Andruh

Received: 31 January 2025
Revised: 11 March 2025
Accepted: 20 March 2025
Published: 24 March 2025

Citation: Maciel, J.W.; Kalinke, L.H.G.; Rabelo, R.; Alvarenga, M.E.; Martins, F.T.; Moliner, N.; Cangussu, D. Slow Relaxation of Magnetization and Magnetocaloric Effects in One-Dimensional Oxamato-Based Lanthanide(III) Coordination Polymers. *Magnetochemistry* **2025**, *11*, 23. https://doi.org/10.3390/magnetochemistry11040023

Copyright: © 2025 by the authors. Licensee MDPI, Basel, Switzerland. This article is an open access article distributed under the terms and conditions of the Creative Commons Attribution (CC BY) license (https://creativecommons.org/licenses/by/4.0/).

1. Introduction

The development of new multifunctional molecular materials (MMMs) is an important field of research due to the ability of these materials to combine different structures and chemical or physical properties for technological innovation. Coordination chemistry offers suitable alternatives for building MMMs for this purpose, such as coordination polymers (CPs). There are already many studies of porosity, good absorption capacity [1,2], and optical [3] and magnetic or magnetocaloric properties [4–6] where the CPs are used. The studies of CPs with 4*f* metal ions have been widely explored due to the enormous potential of working with MMMs that combine, for example, structural diversity with optical and magnetic/magnetocaloric properties [3,7]. The lanthanide(III) ions can show high coordination numbers, which allows different structures topologies for coordination polymers resulting from interaction with different organic ligands. The lanthanide(III) CPs can show good optical and magnetic/magnetocaloric properties depending on the

choice of metal ion and organic ligand. These materials are interesting for applications like optoelectronics, spintronics, and cryogenic magnetic refrigeration [8].

Aromatic polyoxamato ligands have been amply used to obtain CPs with 3*d* metals. The great advantage of this type of ligand is the ability to build CPs with predictable structures and tunable magnetic properties; the ligand can efficiently transmit the magnetic coupling between neighboring metal atoms [9–12]. Many compounds with 4*f* metal ions and aromatic-substituted monooxamato ligands have been reported in the literature, most of which use ligands with monoprotonated oxamato groups. A mononuclear lanthanide(III) oxamato compound exhibiting a single-ion magnet (SIM) behavior is $Me_4N[Dy^{III}(H\text{-}2,6\text{-}dmpa)_4]\cdot 2CH_3CN$ [2,6-dmpa = *N*-2,6-dimethylphenyloxamate]; the hydrogen-bond-mediated self-assembly of this compound in the solid state provides a first example of 2D hydrogen-bonded polymer with a herringbone net topology [9]. Other examples employing the tetrabutylammonium salt of the *N*-(4-chlorophenyl)oxamate ligand (4-Clpa) yielded a series of mononuclear lanthanide(III) complexes of general formula $NBu_4[Ln^{III}(H\text{-}4Clpa)_4(dmso)]$, where Ln = Y, La, Nd, Eu, Gd, Tb, Dy, and Ho. Among these, the Nd, Gd, Tb, and Dy compounds exhibited a field-induced slow relaxation of magnetization typical of SIM behavior [13–15]. Using the sodium salt of the *N*-4-hydroxyphenyloxamate ligand (4-OHpa) towards the Ln(III) ions resulted in a series of a 2D $Na^{I}Ln^{III}$ supramolecular coordination networks, where Ln = Eu, Gd, Dy, and Ho, and only the Gd(III) compound presented a rare slow relaxation of the magnetization [16]. The simpler *N*-phenyloxamate ligand (pa) recently afforded 1D Ln^{III} CPs, where Ln = Eu, Gd, and Tb. These are examples of CPs featuring an aryl-monoxamato ligand without coordinating groups attached to the aromatic ring [17].

Our group's extensive work with the coordination chemistry of the proligand *N*-(4-carboxyphenyl)oxamic acid (H_3pcpa) towards *p*-, *d*-, and *f*-block metal ions has led to the synthesis of a discrete Fe^{III} complex in addition to Pb^{II}, Mn^{II}, Co^{II}, Zn^{II}, Cd^{II}, Eu^{III}, Tb^{III}, and Gd^{III} CPs [18–20]. Their crystal structures revealed diverse coordination and bridging modes of the anionic $Hpcpa^{2-}$ ligand (Scheme 1), highlighting its remarkable versatility in self-assembling CPs with various metal ions.

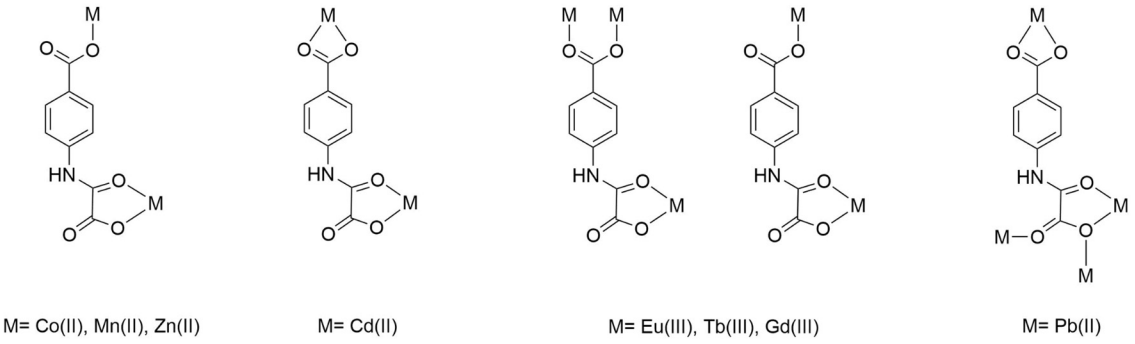

Scheme 1. Different bridging coordinated modes of the monoprotanated *N*-(4-carboxyphenyl)oxamate ligand observed in their metal coordination polymers.

The 1D Eu and Tb CPs of the $Hpcpa^{2-}$ ligand exhibited red and green emission, respectively, with the Tb compound showing a higher quantum yield due to the oxamate ligand's superior sensitization of Tb^{III} ions. In contrast, the Gd analog displays slow magnetic relaxation under an applied field, classifying it as a field-induced single-molecule magnet (SMM) [19]. Focusing on the magnetic and magnetocaloric properties, we present a related series of Ln(III) CPs (Ln = Dy, Ho, and Er) with the $Hpcpa^{2-}$ ligand. Their synthesis, chemical and structural characterization, and the analysis of their magnetic and magnetocaloric properties are reported herein. In this regard, highly anisotropic

holmium(III), dysprosium(III), and erbium(III) ions with $^5I_8$, $^6H_{15/2}$, and $^4I_{15/2}$ ground states, respectively, are particularly well suited to test their magnetocaloric efficiency, when compared with the isotropic gadolinium(III) ion with an orbital-free $^8S_{7/2}$ ground state ($J = 7/2$ with $S = 7/2$ and $L = 0$). They possess the highest value of total angular momentum along the lanthanide(III) series because of the first-order spin-orbit coupling (SOC) effects of the $4f^9$ Dy^{III} ($J = 15/2$ with $S = 5/2$ and $L = 5$), $4f^{10}$ Ho^{III} ($J = 8$ with $S = 2$ and $L = 6$), and $4f^{11}$ Er^{III} ions ($J = 15/2$ with $S = 3/2$ and $L = 6$).

2. Experimental Section

2.1. General Information

All manipulations were carried out under aerobic conditions. Chemicals were purchased from Sigma-Aldrich and used without further purification. The synthesis of the *N*-(4-carboxyphenyl)oxamic acid ethyl ester (EtH_2pcpa) and Na_2Hpcpa were performed following the previous report [18–21]. Elemental analysis (C, H, and N) was performed by Fisons EA1108. Solid-state infrared spectra were recorded on a Perkin Elmer Spectrum 400 FT-IR/FT-FIR spectrometer using KBr in the 400–4000 cm^{-1} range, and 1H NMR were conducted by the Microanalytical Service of the Central de Análises Multiusuária of Federal University of Goiás. Thermogravimetric (TG) analysis was performed using samples obtained from the polycrystalline synthesis. The analyses were carried out at the Regional Center for Technological Development and Innovation (CRTI) on a Netzsch STA 449 F3 Nevio instrument over a temperature range of 30 to 650 °C, with a heating rate of 10 °C per minute under a synthetic air atmosphere. Powder X-ray diffraction (PXRD) data were collected for polycrystalline powders at CRTI using a Bruker D8 Discover powder diffractometer, using Cu-Kα radiation at a voltage of 40 kV and a current of 40 mA in the 2θ range 3.00–50.00° with a step-size of 0.0151°. The samples were kept at 15 rpm rotations during a measurement.

2.2. Synthesis

$\{[Ln_2(Hpcpa)_3(H_2O)_5]\}_n$ [Ln = Dy^{III} (**1**), Ho^{III} (**2**) and Er^{III} (**3**)] were prepared by two different methods. The first method involved slow diffusion techniques in H-shaped tubes as follows: aqueous solutions of $Dy(NO_3)_3$ (0.1 mmol, 0.0348 g), $HoCl_3{\cdot}6H_2O$ (0.1 mmol, 0.0379 g), and $Er(NO_3)_3{\cdot}5H_2O$ (0.1 mmol, 0.0443 g) were placed in one arm of the corresponding H-tube, whereas an aqueous solution of Na_2Hpcpa (0.1 mmol, 0.037 g) was placed in the other arm. Water was added dropwise to fill the H-tube, which was covered with parafilm and allowed to stand at room temperature. All tubes yielded crystals; however, not all were suitable for single-crystal X-ray diffraction analysis. The second method involved mixing a solution of the rare-earth metal salt with a solution of the ligand salt in a 2:3 metal-to-ligand molar ratio. This process resulted in a polycrystalline solid, which was filtered and dried under vacuum. The yields were 78%, 81%, and 83% for **1**–**3**, respectively. Elemental analysis (C,H,N) Calcd for $C_{27}H_{25}Dy_2N_3O_{20}$ (**1**): C 31.29; H, 2.43; N, 4.05. Found: C 30.74; H, 2.72; N, 4.04%. Anal. Calcd for $C_{27}H_{25}Ho_2N_3O_{20}$ (**2**): C, 31.14; H, 2.42; N, 4.04. Found: C 30.62; H, 2.61; N, 3.94%. Anal. Calcd for $C_{27}H_{25}Er_2N_3O_{20}$ (**3**): C 31.00; H, 2.41; N, 4.02. Found: C 30.47; H, 2.59; N, 4.05%. Selected IR data (KBr disk, cm^{-1}): 3425(br), 1651(s), 1604(s), 1537(s), 1412(s), 1311(w), 1182(w), 862(w), and 786(m) for **1**; 3419(br), 1651(s), 1604(s), 1538(s), 1415(s), 1311(w), 1182(w), 862(w), and 786(m) for **2**. 3434(br), 1650(s), 1604(s), 1539(s), 1415(s), 1311(w), 1182(w), 862(w), and 786(m) for **3**.

2.3. Crystallographic Data Collection and Refinement

All reflections for single crystals of **3** were collected on a Bruker-AXS Kappa Duo diffractometer (Billerica, MA, USA) equipped with an APEX II CCD detector with either Mo

Kα (λ = 0.71073 Å). The structure was solved by direct methods through SHELXS-2014 [22] of phase retrieval and then refined by full-matrix least-squares on F^2 with anisotropic thermal parameters for all non-hydrogen atoms, while the hydrogen atoms were stereochemically positioned and their displacement parameters fixed and set to isotropic [U_{iso} (H) = 1.2Ueq (CH or NH) or 1.5Ueq (water)]. In addition, some scattered peaks with residual electron density were still observed in the difference Fourier map located in a void for **3**. Attempts were made to assign these peaks as nonstoichiometric water molecules; however, checkcif alerts arise, such as short distances with other atoms, like coordination water molecules. Therefore, PLATON/SQUEEZE [23] was used to remove their contribution to the diffraction data. The Mercury [24] and ORTEP-3 [25] programs were used within the WinGX [26] software version 4.0 package to prepare artwork representations. Crystallographic data and refinement parameters of **3** are summarized in Table 1, whereas selected bond distances and angles are listed in Table S2 and Table S3, respectively. All crystallographic data are available from the CCDC. The CCDC number is 2417034 (**3**).

Table 1. X-ray diffraction data collection and refinement parameters for **3**.

	3
Empirical formula	$C_{27}H_{25}N_3O_{20}Er_2$
Formula weight	1046.02
Crystal system	Monoclinic
Space group	Cc
a/Å	24.290(4)
b/Å	19.873(4)
c/Å	7.4327(13)
β/°	104.998(5)
V/Å^3	3465.7(11)
Z	4
T/K	296
Radiation	Mo Kα
Wavelength/Å	0.71073
ρ/g cm^{-3}	2.005
μ//mm^{-1}	4.897
Symmetry factor (Rint)	0.1171
Completeness to θmax/%	98.70
F(000)	2016.0
Refined parameters	272
Reflections collected	6351
R [a], wR [b] [I > 2s(I)]	0.1087, 0.3155
R [a], wR [b] (tall data)	0.1502
S [c]	1.127
ρ_{max} and ρ_{min}/*e*Å^{-1}	2.3400/–4.2300
CCDC	2417034

[a] $R = S\,||F_o| - |F_c||/S\,|F_o|$. [b] $wR = [S\,w(|F_o|^2 - |F_c|^2)^2/S\,w|F_o|^2]^{1/2}$. [c] $S = [S\,w(|F_o|^2 - |F_c|^2)^2/(n_o - np)]^{1/2}$, where $w \propto 1/s$, n_o = observed, and n_p = fitted parameters.

2.4. Magnetic Measurements

Variable-temperature (2–300 K) direct-current (dc) magnetic susceptibility measurements under an applied magnetic field of 0.5 T and variable-temperature (2–10 K) and variable-field (0–5 T) magnetization measurements were carried out using a Quantum Design Superconducting Quantum Interference Device (SQUID) magnetometer.

Variable-temperature (2–16 K) and variable-field (0–0.25 T) alternating-current (ac) magnetic susceptibility measurements under a ±5.0 Oe oscillating field at frequencies in the range 0.1–10 kHz were performed with a Quantum Design Physical Property Measurement

System (PPMS). The magnetic measurements, performed on powdered samples embedded in eicosane to prevent any crystal reorientation, were corrected for the diamagnetism of the constituent atoms and the sample holder.

3. Results

3.1. Syntheses and General Physicochemical Characterization of **1**–**3**

The preparation of **1**–**3** was performed by slow diffusion in the H tube that yielded X-ray quality single crystals for **3** and polycrystalline samples for **1** and **2**. All of them were also prepared using the precipitation method with good yields. The infrared spectra of the complexes can be seen in Figure S1. All compounds present characteristic bands of the ligand such as stretching of the C=O amide bond and C–H and C=C phenyl bonds. They also show strong absorptions in the high-frequency region above 3400 cm^{-1} due to stretching vibrations of the O–H bond of crystallization and coordination water molecules involved in hydrogen bonding. At the same region, superimposed on the broad O–H stretching band, it is possible to observe a narrow band of N–H stretching, thus being an indication that the nitrogen of the oxamate group is not involved in metal coordination. The PXRD patterns for the polycrystalline samples of **1**–**3** (Figure 1) indicated that all compounds were isostructural, possessing the same structure of **3** described below, and confirmed the phase purity of the compounds.

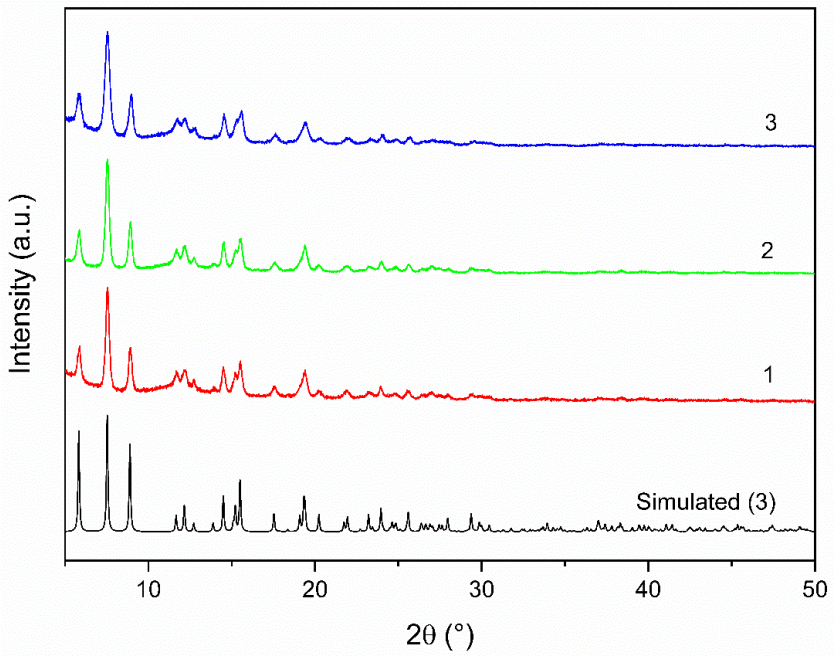

Figure 1. Experimental PXRD patterns for **1**–**3** and simulated one for **3**.

The TG curves (Figure S2) of **1**–**3** are similar. They lose about 10% of their weight up to 170 °C, which can be attributed to the loss of six water molecules [calculated/found = 10.2/10.9 (**1**), 10.2/10.5, (**2**) and 10.1/9.7 (**3**)]. This first mass loss is followed by an almost plateau up to 350 °C. Two major mass losses occur between 350 and 450 °C due to the decomposition of the anhydrous phases. The final waste from thermal decomposition can be attributed to the respective lanthanide oxides (Ln_2O_3).

The electronic spectra in the UV-vis-NIR region of **1**–**3** were collected at room temperature (Figure S3). The diffuse reflectance spectra display characteristic absorption lines of 4f transitions [27–29] of the Dy^{III}, Ho^{III} and Er^{III} ions [**1**: $^6H_{15/6} \rightarrow {}^6H_{7/6} + {}^6F_{9/2}$ (1106 nm), $^6H_{15/6} \rightarrow {}^6F_{7/2}$ (910 nm), $^6H_{15/6} \rightarrow {}^6F_{5/2}$ (807 nm), $^6H_{15/6} \rightarrow {}^6F_{3/2}$ (756nm), $^6H_{15/6} \rightarrow {}^4F_{9/2}$ (474 nm), $^6H_{15/6} \rightarrow {}^4I_{15/2}$ (463 nm), and $^6H_{15/6} \rightarrow {}^4G_{11/2}$ (427 nm); **2**: $^5I_8 \rightarrow {}^5I_6$ (1159 nm),

$^5I_8 \rightarrow {}^5I_5$ (897 nm), $^5I_8 \rightarrow {}^5I_4$ (753 nm), $^5I_8 \rightarrow {}^5F_5$ (643 nm), $^5I_8 \rightarrow {}^5S_2$ (538 nm), $^5I_8 \rightarrow {}^5F_4$ (486 nm), $^5I_8 \rightarrow {}^5F_3$ (474 nm), $^5I_8 \rightarrow {}^5F_2$ (468 nm), $^5I_8 \rightarrow {}^5G_6$ (450 nm), $^5I_8 \rightarrow {}^5G_5$ (418 nm), $^5I_8 \rightarrow {}^5G_4$ (386 nm), and $^5I_8 \rightarrow {}^3K_7$ (382 nm); **3**: $^4I_{15/2} \rightarrow {}^4I_{11/2}$ (980 nm), $^4I_{15/2} \rightarrow {}^4I_{9/2}$ (802 nm), $^4I_{15/2} \rightarrow {}^4F_{9/2}$ (652 nm), $^4I_{15/2} \rightarrow {}^4S_{3/2}$ (544 nm), $^4I_{15/2} \rightarrow {}^4H_{11/2}$ (520 nm), $^4I_{15/2} \rightarrow {}^4F_{7/2}$ (488 nm), $^4I_{15/2} \rightarrow {}^4F_{5/2}$ (451 nm), $^4I_{15/2} \rightarrow {}^4F_{3/2}$ (444 nm), $^4I_{15/2} \rightarrow {}^4H_{9/2}$ (407 nm), and $^4I_{15/2} \rightarrow {}^4G_{11/2}$ (378 nm)].

3.2. Description of the Structure of **3**

The crystallographic results reveal that **3** crystallizes in the monoclinic *Cc* space group and forms zig–zag chains parallel to the crystallographic b axis [101] direction, as shown in Figure 2. The asymmetric dinuclear unit, shown in Figure 2a, consists of two crystallographically independent Er^{III} ions (Er1 and Er2), three anionic $Hpcpa^{2-}$ ligands, and five coordinated water molecules. The Er1 and Er2 ions exhibit eight-coordination, with three (Er1) or two (Er2) water molecules, four (Er1) or three (Er2) carboxylate oxygen atoms, and one (Er1) or two (Er2) amide oxygen atoms, defining a geometry intermediate between triangular dodecahedron (D_{2d}), square antiprism (D_{4d}), and biaugmented trigonal prism (C_{2v}), as determined by the SHAPE program (see Table S1). The Er1−O bond lengths range from 2.24(3) to 2.63(3) Å, while the Er2−O bond lengths range from 2.27(3) to 2.58(3) Å (see Table S2). Additionally, the Er^{III}−O (water) and Er^{III}−O (oxamate) distances are consistent with previously reported structures. The O−Er^{III}−O bond angles range from 60.4(8)° to 147.9(10)° (see Table S2). These angles were comparable with related compounds reported in the literature.

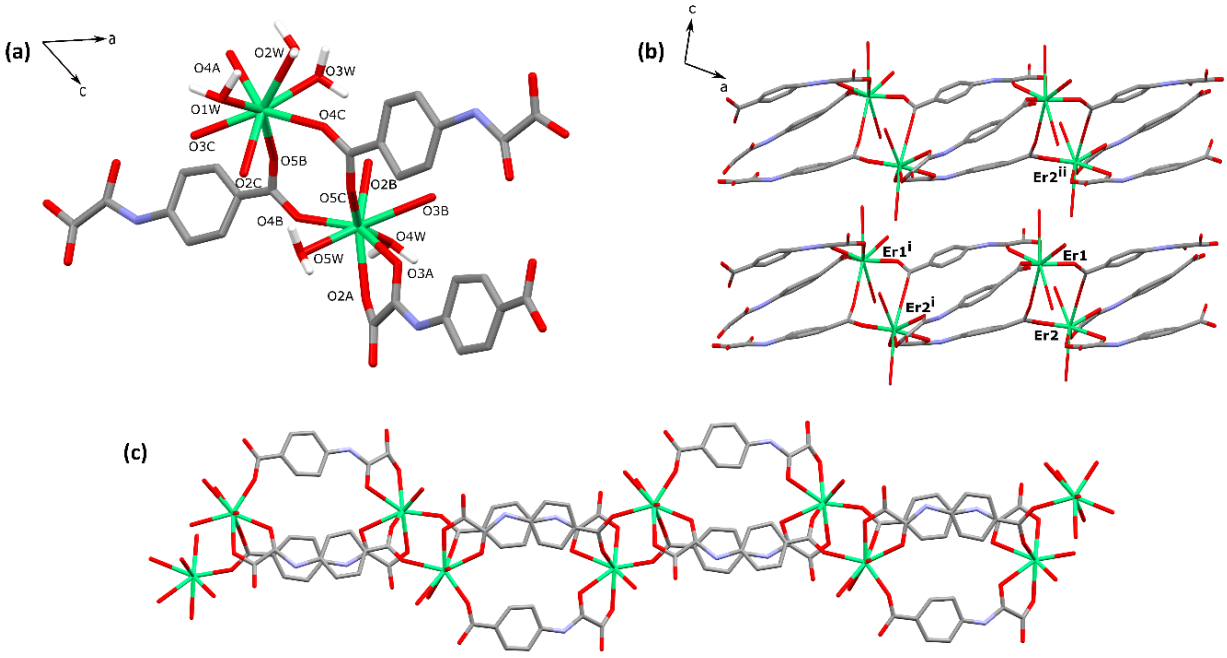

Figure 2. (**a**) A view of the asymmetric unit of **3** with the atom numbering of the metal environment. (**b**) A view of the arrangement of two neighboring chains parallel to the *ac* plane. (**c**) A perspective view of a fragment of the zigzag chain of **3** running along the crystallographic *a*-axis. Color code: C (gray), N (blue), O (red), Er (green), and H (white). Symmetry code: (i) = ½ + *x*, ½ *y*, ½ + *z*; (ii) = *x*, −*y*, ½ + *z*.

Double *syn*−*syn* carboxylate(oxamate) groups connect Er1 and Er2 into pairs within each chain, the erbium−erbium separation being 4.961(4) Å for Er1···Er2. These dinuclear units are, in turn, interlinked by three $Hpcpa^{2-}$ ligands, one of them through the μ-κ^{2}O,O′:κO″ coordination mode and the other two across the μ_3-κ^{2}O,O′:κO″:κO‴ one, resulting in neutral 1D CPs (Figure 2b). Two root mean square deviation (rmsd) planes

were fitted through the atoms that connect the erbium cations across the oxamate bridge in the double syn−syn conformation cited above. The planes were defined as A and B and fitted through the C6B,C9B,O4B,O5B and C6C,C9C,O4C,O5C sets of atoms, respectively.

Within the resulting triple-stranded moieties, the values of the metal–metal distances through these extended μ-κ^{2}O,O′:κO″- and μ$_3$-κ^{2}O,O′:κO″:κO‴-Hpcpa^{2-} bridges are 10.152(2), 12.227(5), and 12.220(6) Å for Er1···Er2^{i}, Er1···Er1^{i} and Er2···Er2^{i} [symmetry operations (^{i}): = ½ + *x*, ½ − *y*, ½ + *z*], respectively (Figure 2c). Additionally, the interaction between two parallel chains through hydrogen bonds and π−π interactions results in a supramolecular 2D network (Figure 3) in which the shortest interlayer contact between the erbium atoms is 6.075(3) Å [Er1 and Er2^{ii}, symmetry operations (^{ii}): = *x*, −*y*, ½ + *z*]. These π−π interactions occur along the crystallographic *c* axis with values of the distance between centroids of 3.717 (2) Å (see Figure 3a).

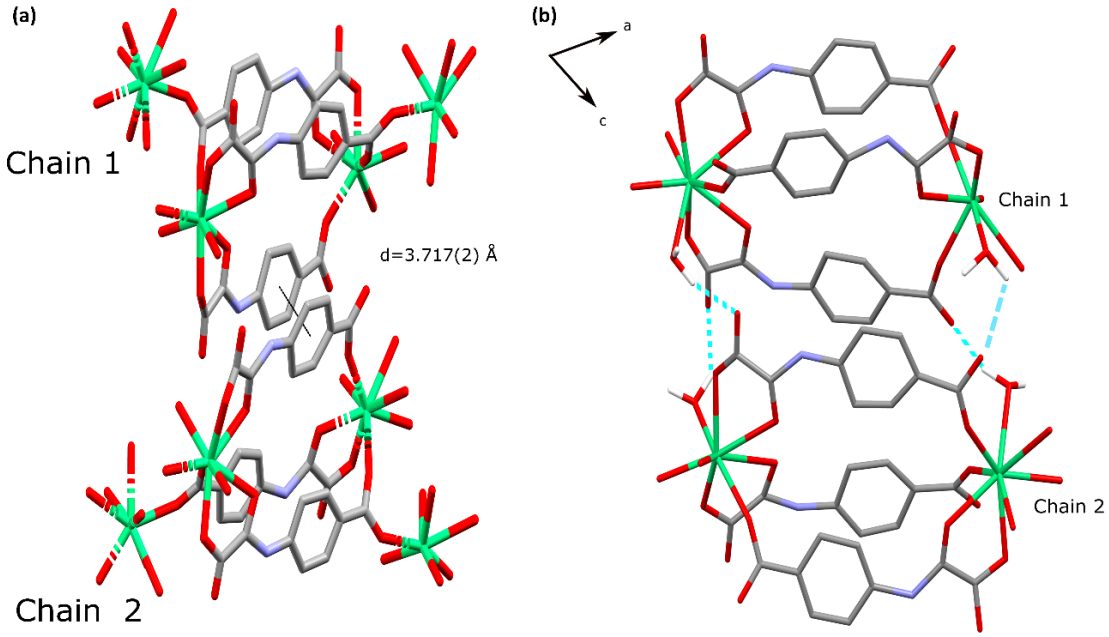

Figure 3. Intermolecular interactions between two parallel chains of **3** through (**a**) π-π stacking showing the distance between the centroid of the aromatic rings along the crystallographic *c*-axis and (**b**) hydrogen bonds between coordinated water molecules and oxygen atoms from the two Hpcpa^{2-} bridges along *b*-axis. Some hydrogen atoms were omitted for clarity. Dashed cyan and black lines represent hydrogen bonds and π-π interactions, respectively.

The interaction between two chains is established by hydrogen bonds interactions, which occur along the *b* and *c* axes. The connection between two chains through O−H···O hydrogen bonds along the *b* axis can be observed in Figure 3. These intermolecular interactions involve oxygen atoms belonging to coordinated water molecules (O1W, O2W, O3W, O4W, and O5W) and oxamate oxygen atoms (O1B and O2B). The connection between the chains is also observed along the *c* axis (Figure 3b). These interactions involve coordinated water molecules (O1W, O2W, O4W, and O5W) and oxamate oxygen atoms (O1A, O2A, O5A, and O2C). The molecular contacts include O−H···O interactions that are mainly established by water molecules and oxamate oxygen atoms. The geometric parameters of the hydrogen bond interactions for **3** are summarized in Table S3.

3.3. Magnetic Properties of **1**–**3**

The dc magnetic properties of **1**–**3** in the form of the $\chi_M T$ vs. T plots [where χ_M represents the dc magnetic susceptibility per two lanthanide(III) ions] are presented in

Figure S4. At 300 K, the $\chi_M T$ values are 27.0 (**1**), 27.3 (**2**), and 21.5 cm^3 mol^{-1} K (**3**). Such values are close to the calculated value for two magnetically isolated Ln^{III} ions with $^5I_8$ (Ln = Ho), $^6H_{15/2}$ (Ln = Dy), and $^4I_{15/2}$ (Ln = Er) ground states, well separated from the low-lying excited states. Then, $\chi_M T$ decreases with decreasing temperature due to the thermal depopulation of the M_J states resulting from the ligand field (LF) splitting, reaching values of 15.1 (**1**), 10.0 (**2**) and 9.3 cm^3 mol^{-1} K (**3**) at 1.9 K. However, the occurrence of antiferromagnetic interactions between the Ln^{III} ions through the double *syn*−*syn* carboxylate bridge cannot be discarded [16]. The normalized isothermal magnetization (*M* vs. *H*/*T*) curves do not superimpose below 10 K in agreement with the strong magnetic anisotropy of these ions, as shown in the inset of Figure S4.

The ac magnetic properties of **1**–**3** were investigated under different applied dc magnetic fields (*H* = 0, 0.1 and 0.25 T). Their behaviors are shown in Figures 4, S5 and S6 in the form of χ_M' and χ_M'' vs. *T* or ν plots [χ_M' and χ_M'' being the in-phase and out-of-phase ac molar magnetic susceptibilities per two lanthanide(III) ions, *T* the temperature, and ν the frequency of the oscillating ac field]. Even though the static dc magnetic properties of **1**–**3** are similar, that is not the case concerning their dynamic ac magnetic properties. Neither the frequency dependence of χ_M' nor a χ_M'' signal was observed for **2**. However, slow magnetic relaxation phenomena occur in **1** and **3**. While in **3**, only field-induced incipient signals of χ_M' and χ_M'' are observed by applying a *H*, **1** exhibits frequency- and temperature dependence of the χ_M' and χ_M'' even in the absence of *H*, which varies significantly by changing the *T*, ν, or *H*. Only incipient χ_M'' signals are observed for **1** under *H* = 0 or 0.1 T [Figure 4a,b(right)], while χ_M'' maxima arise under *H* of 0.25 T [Figure 4c(right)]. For instance, these maxima slightly shift toward higher temperatures with increasing ν from 0.1 to 1 kHz but revert with the further increase in ν up to 10 kHz. This uncommon behavior noted for the χ_M'' vs. *T* plots was described by Boča and collaborators as a phenomenological "reciprocating thermal behavior" due to a "strange" relaxation mechanism [30].

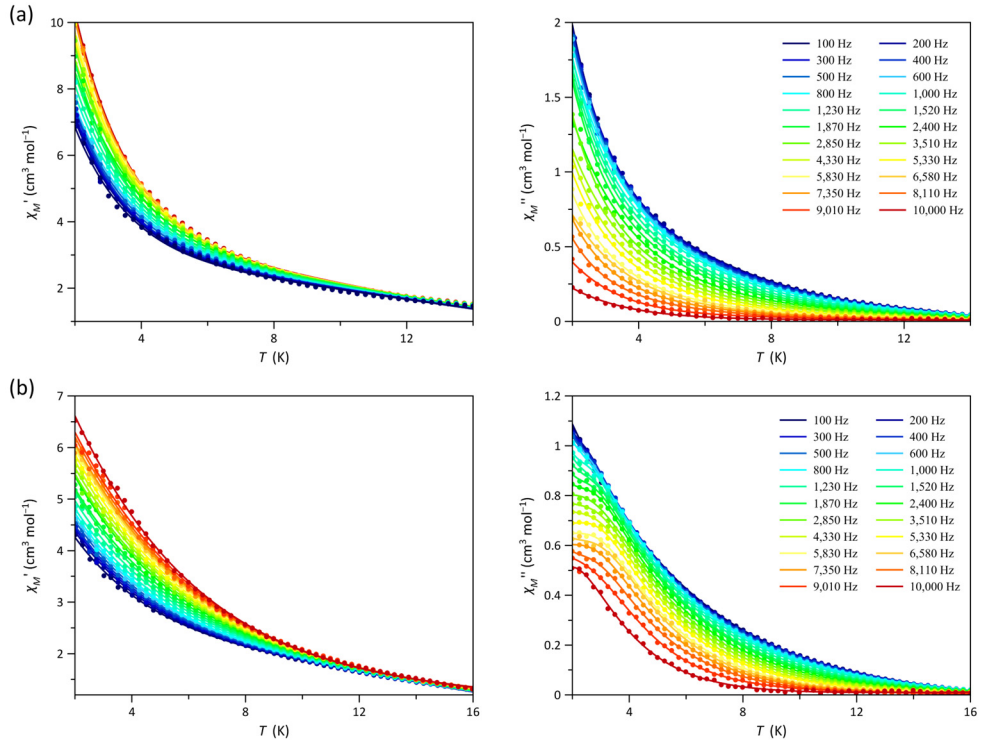

Figure 4. *Cont.*

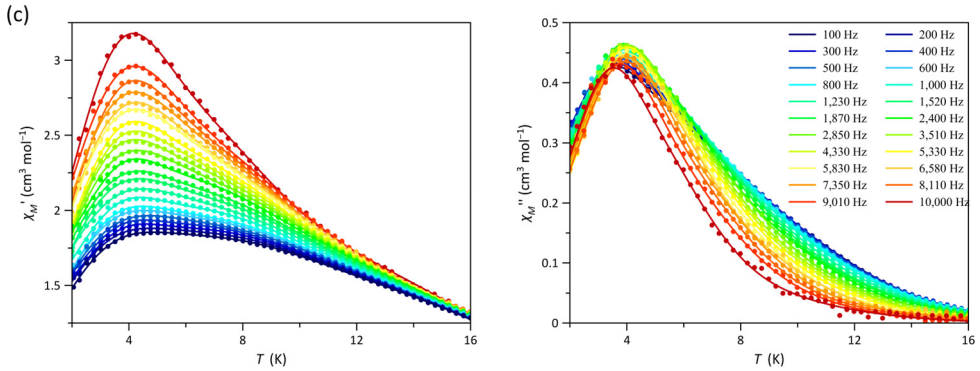

Figure 4. Temperature dependence of $\chi_M{}'$ (**left**) and $\chi_M{}''$ (**right**) for **1** at a 5.0 G oscillating field in the frequency range of 0.1–10 kHz (red to blue) in the absence of applied static magnetic fields (**a**) and under 0.1 (**b**) and 0.25 T (**c**). The solid lines are only eye guides.

Unfortunately, the incipient nature of the data prevented accurate analysis of most of the ac magnetic measurements. Thus, only the magnetic relaxation time (τ) values for **1** at H = 0.25 T were extracted by fitting the $\chi_M{}'$ and $\chi_M{}''$ vs. ν plots through the generalized Debye model [31]. They are shown as an Arrhenius plot in Figure 5. At higher temperatures (above 5 K), the experimental data follow an Arrhenius law of a thermally activated magnetic relaxation process referring to the climbing of the energy barrier to spin reversal. However, below 5 K, the relaxation process speeds up again upon cooling, and the "strange" mechanism becomes a more efficient path for the spin reversal. So, the experimental relaxation times can be satisfactorily simulated through a model that considers a two-phonon Orbach mechanism [$\tau^{-1} = {\tau_0}^{-1} \exp(-U_{\text{eff}}/k_{\text{B}}T)$] plus a "strange" one [$\tau^{-1} = FT^{-k}$, with $k > 0$]. The best-fit values of τ_0 and U_{eff} [1.50(3) $\times$ 10^{-6} s and 14.81(13) cm^{-1}] are within the range found in other Dy(III) compounds [32]. Meanwhile, the found values of F and k are 1.96(4) $\times$ 10^6 K^k s^{-1} and 4.2(2), respectively. Only two examples were reported in the literature: a dinuclear {Ni$^{\text{II}}$Gd$^{\text{III}}$} complex with a Schiff's Base ligand and a Dy$^{\text{III}}$ chain represented by the formulas [Ni(*vanen*)Gd(H$_2$O)Cl$_3$] and [Dy(DPOA)(NO$_3$)(H$_2$O)$_2$]$_n$·nH$_2$O. For the Dy compound, the reported parameters related to the "strange" mechanism [$\tau^{-1} = FT^{-k}$, with $k > 0$] are F = 1.0 $\times$ 10^4 K^k s^{-1} and k = 2.8, values comparable to those found for compound **1** in our work [30]. Still, it is hard to argue on those "strange" parameters since, to date, this type of relaxation mechanism has only a phenomenological meaning.

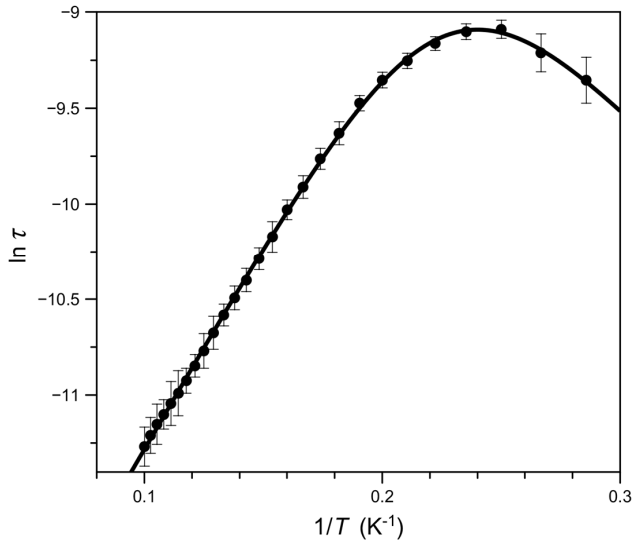

Figure 5. Arrhenius plots for **1** under applied dc magnetic field of 0.25 T. The solid line is the best-fit curve (see text).

3.4. Magnetocaloric Properties of **1**–**3**

The magnetocaloric effect (MCE) of **1**–**3** has been investigated by variable-temperature (T = 2–10 K) and variable-field (H = 0–5 T) magnetization measurements (see Section 2). The field and temperature dependence of the magnetic entropy change (ΔS_m) upon connecting the magnetic field ($\Delta H = H - H_0$ with $H_0 = 0$) has been estimated from the M vs. H and T plots (M being the gravimetric magnetization) according to the Maxwell equation (Figure 6), as reported elsewhere [33,34].

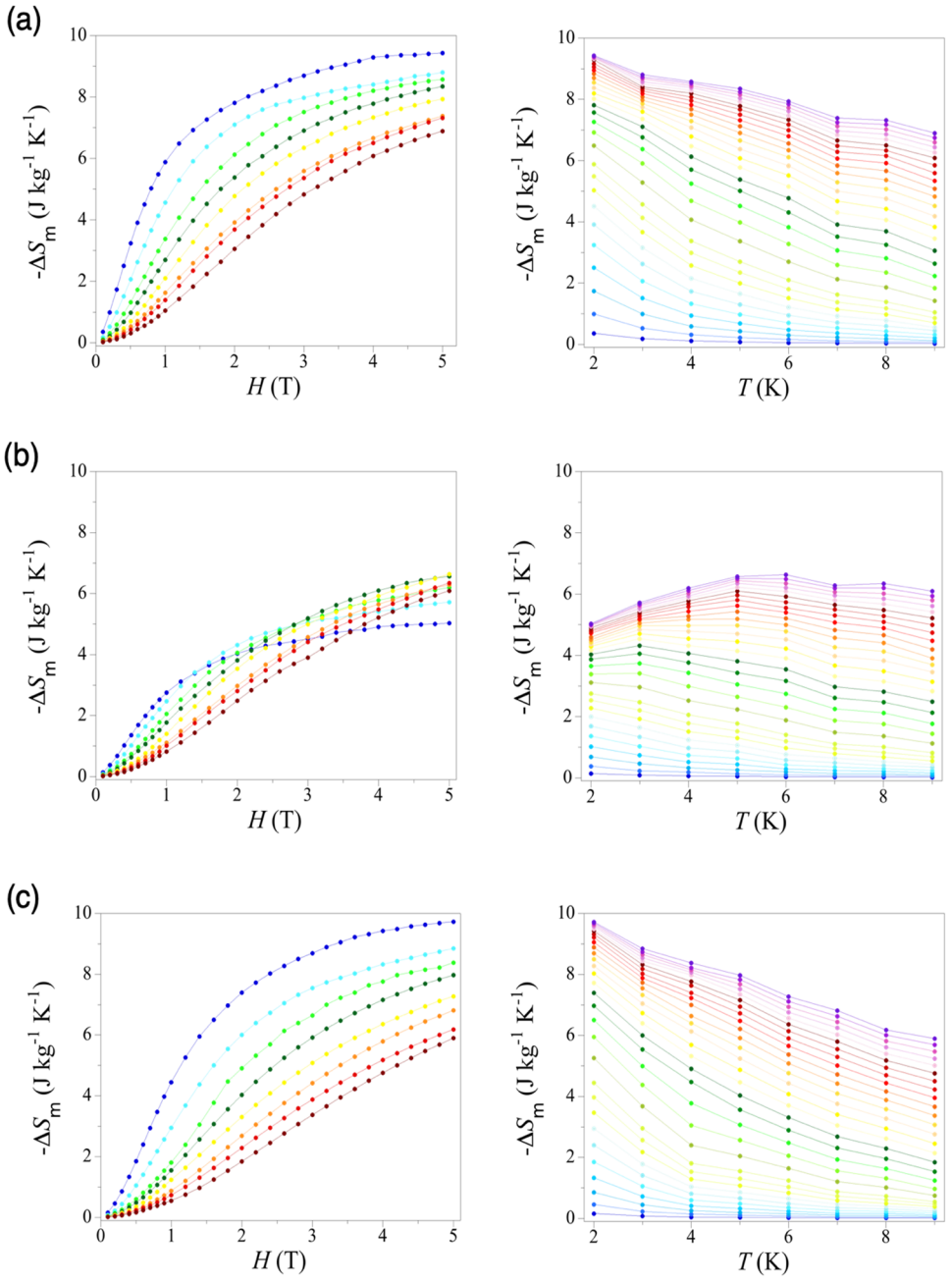

Figure 6. Field (**left**) and temperature (**right**) dependence of $-\Delta S_m$ for **1** (**a**), **2** (**b**), and **3** (**c**) in the temperature and field range of 2.0–10 K (blue to red) and 0–5 T (blue to purple), respectively. The solid lines are only eye guides.

The $-\Delta S_m$ vs. H and T plots show a monotonic increase with decreasing the temperature or increasing the field for **1** and **3** (Figure 6a and c, respectively), whereas **2** evidences a decrease upon cooling further for $T < 5$ K with the progressive development of a maximum

from 3 up to 6 K for $\Delta H > 2$ T (Figure 6b). Interestingly, the $-\Delta S_m$ maxima for **2** occur for $\Delta H > 2$ T, whereas it does not show slow magnetic relaxation effects above 2 K. In contrast, no $-\Delta S_m$ maxima are observed for **1** and **3** for $\Delta H < 5$ T, evidencing thus that the blockage of the magnetization that occurs at low temperatures under the application of a weak *dc* magnetic field [$T_B < 4.5$ (**1**) and 3.5 K (**3**) for $H = 0.025$ T] does not preclude the observation of a significant MCE along this series.

The maximum $-\Delta S_m$ value in gravimetric units for $\Delta H = 5$ T increases from **2** to **1** and **3** [9.4 (**1**)/6.6 (**2**)/9.7 J kg^{-1} K^{-1} (**3**) at $T = 2$ (**1**)/6 (**2**)/2 K (**3**)], being comparable to those of the gadolinium(III)–gallium(III) garnet used as commercial cryogenic material [$-\Delta S_m = 6.5$ and 28.0 J kg^{-1} K^{-1} at $T = 2$ and 10 K, respectively, for ΔH = 8 T] [35]. Moreover, the corresponding $-\Delta S_m$ value for $\Delta H = 1$ T [5.8 (**1**)/1.4 (**2**)/4.4 J kg^{-1} K^{-1} (**3**) at $T = 2$ (**1**)/6 (**2**)/2 K (**3**)] reaches up to 62 (**1**), 21 (**2**), and 45% (**3**) of the maximum $-\Delta S_m$ value. This relatively weak magnetic field is close enough to the stronger field to be achieved with the standard permanent magnets used commercially (ranging from 0.5 to 1 T for ceramic magnets and up to 1.4 T for neodymium ones). These two features (high magnetic entropy changes and large slope of the corresponding isothermal magnetic entropy variation curves) are mandatory for potential applications in CMR.

The overall enhancement of the MCE in the order **2** < **1** ≈ **3** is likely explained by the larger magnetic anisotropy of the 4f^{10} Ho^{III} ion ($^5I_8$) compared to the 4f^9 Dy^{III} ($^6H_{15/2}$) and 4f^{11} Er^{III} ($^4I_{15/2}$) ions, despite the larger *J* value in the former case. Indeed, the maximum $-\Delta S_m$ values in molar units [9.7 (**1**)/6.9 (**2**)/10.1 J mol^{-1} K^{-1} (**3**) at $T = 2$ (**1**)/6 (**2**)/2 K (**3**) for ΔH = 5 T] are somewhat lower than the limiting values for two magnetically isolated Ln^{III} ions with no zero-field splitting (*zfs*) [$-\Delta S_m = 2R\ln(2J + 1) = 46.1$ (Dy)/47.1 (Ho)/46.1 J mol^{-1} K^{-1} (Er) with $J = 15/2$ (Dy), 8 (Ho), and 15/2 (Er)]. By comparison, the $-\Delta S_m$ values in molar units (per mol of lanthanide atom) [3.0 (**1**)/0.7 (**2**)/2.3 J mol^{-1} K^{-1} (**3**) at $T = 2$ (**1**)/6 (**2**)/2 K (**3**) for $\Delta H = 1$ T] are similar to those reported for the gadolinium(III)–gallium(III) garnet and its dysprosium(III)-substituted derivatives of general formula $(Dy_xGd_{1-x})_3Ga_5O_{12}$ [$x = 0$ (GGG), 0.5 (DGGG), and 1 (DGG)] [$-\Delta S_m = 3.1$–3.3 J mol^{-1} K^{-1} at $T = 5$ K for $\Delta H = 2$ T] [36].

In this respect, the MCE efficiencies for **1**–**3** are comparable to those of related magnetically anisotropic lanthanide(III) metal–organic frameworks (MOFs) and its mixed gadolinium(III)-substituted heterometallic derivatives of general formula $[(Ln_xGd_{1-x})(HCO_2)_3]_n$, $[(Ln_xGd_{1-x})(HCO_4)]_n$, $[(Ln_xGd_{1-x})_3(ad)_{4.5}(DMF)_2]_n$, and $[(Ln_xGd_{1-x})_3(cb)_4(NO_3)(DMF)_y]_n$ [ad = adipate and cb = 1,7-di(4-carboxyphenyl)-1,7-dicarba-*closo*-dodecaborane with Ln = Eu, Tb, Dy, Ho, Er ($x = 0$–1)], which have been recently proposed as efficient molecular cryomagnetic refrigerants [37–41] in place of traditional purely inorganic intermetallic alloys and oxides, such as mixed lanthanide-transition metal antimonides and tellurides, Ln_6MSb_2 and Ln_6MTe_2 (Ln = Gd, Tb, and Dy; M = Mn, Fe, Co, and Ni), or lanthanide–gallium garnets, $Ln_3Ga_5O_{12}$ (Ln = Gd, Tb, Dy, and Nd) [42,43].

4. Conclusions

The magnetic properties of **1**–**3** are very variable. Although the dc magnetic susceptibility measurements reveal similar trends for all compounds, the ac magnetic properties diverge, with only compounds **1** and **3** displaying slow magnetic relaxation phenomena. The temperature- and frequency-dependent ac susceptibility behavior in **1** is especially remarkable due to a "strange" relaxation mechanism, which has been phenomenologically described but not fully understood to date. This isostructural series of oxamato-based Ln^{III} CPs also exhibits weak (Ln = Ho) to moderate (Ln = Dy and Er) MCE with magnetic entropy change maxima at relatively high temperatures (Ln = Ho), far above He liquefaction.

These findings reinforce the potential of lanthanide-based compounds as efficient molecular cryomagnetic refrigerants, comparable to traditional materials such as

gadolinium–gallium garnets, as new optional materials for magnetic refrigeration technology. Further exploration of the "strange" relaxation mechanism and its impact could lead to new insights in understanding some enigmatic features of the slow magnetic relaxation phenomena.

Supplementary Materials: The following supporting information can be downloaded at: https://www.mdpi.com/article/10.3390/magnetochemistry11040023/s1. Table S1. Analyses of coordination geometry for each LnIII ion in 3. Table S2. Selected bond lengths (Å) and angles (°) for 3. Table S3. Hydrogen bonds in 3. Figure S1. Infrared spectra of 1–3 (top to bottom). Figure S2. Termogravimetric curves for (red line) 1, (green line) 2 and (blue line) 3. Figure S3. Powder diffuse reflectance spectra of 1–3. Figure S4. Temperature dependence of χMT for 1–3 (a-c). The inset shows the M vs H/T plots in the temperature range of 2.0–10 K. Figure S5. Temperature dependence of $\chi M'$ (a) and $\chi M''$ (b) for 3 at a 5.0 G oscillating field in the frequency range of 0.5–10.0 kHz (yellow to blue) under an applied static magnetic field of 0.25 T. Figure S6. Frequency dependence of $\chi M'$ (a) and $\chi M''$ (b) and Argand plots (c) for 1 at a 5.0 G oscillating field in the temperature range of 3.5–10 K under an applied static magnetic field of 0.25 T and frequencies of 0.1–10 kHz (gray to brown).

Author Contributions: Conceptualization, D.C.; methodology, J.W.M. and L.H.G.K.; formal analysis, J.W.M., F.T.M., M.E.A., N.M. and R.R.; investigation, J.W.M., L.H.G.K. and R.R.; data curation, J.W.M., M.E.A. and R.R.; writing—original draft preparation, D.C., J.W.M., L.H.G.K. and R.R.; writing—review and editing, J.W.M. and R.R. All authors have read and agreed to the published version of the manuscript.

Funding: This research was funded by CAPES nº 88887798611/2022-00, CNPq nº 305691/2022-8 and FAPEG project nº 202410267000958.

Institutional Review Board Statement: Not applicable.

Informed Consent Statement: Not applicable.

Data Availability Statement: The original contributions presented in this work are included in the article and Supplementary Materials. Further inquiries can be directed to the corresponding authors.

Acknowledgments: J.W.M. thanks CAPES for the doctoral grant.

Conflicts of Interest: The authors declare no conflicts of interest.

References

1. Wang, T.; Lin, E.; Peng, Y.L.; Chen, Y.; Cheng, P.; Zhang, Z. Rational Design and Synthesis of Ultramicroporous Metal-Organic Frameworks for Gas Separation. *Coord. Chem. Rev.* **2020**, *423*, 213485. [CrossRef]
2. Wang, C.; Liu, X.; Keser Demir, N.; Chen, J.P.; Li, K. Applications of Water Stable Metal–Organic Frameworks. *Chem. Soc. Rev.* **2016**, *45*, 5107–5134. [CrossRef]
3. Liu, J.Q.; Luo, Z.D.; Pan, Y.; Kumar Singh, A.; Trivedi, M.; Kumar, A. Recent Developments in Luminescent Coordination Polymers: Designing Strategies, Sensing Application and Theoretical Evidences. *Coord. Chem. Rev.* **2020**, *406*, 213145. [CrossRef]
4. Zheng, Y.-Z.; Zheng, Z.; Chen, X.-M. A Symbol Approach for Classification of Molecule-Based Magnetic Materials Exemplified by Coordination Polymers of Metal Carboxylates. *Coord. Chem. Rev.* **2014**, *258–259*, 1–15. [CrossRef]
5. Journaux, Y.; Ferrando-Soria, J.; Pardo, E.; Ruiz-Garcia, R.; Julve, M.; Lloret, F.; Cano, J.; Li, Y.; Lisnard, L.; Yu, P.; et al. Design of Magnetic Coordination Polymers Built from Polyoxalamide Ligands: A Thirty Year Story. *Eur. J. Inorg. Chem.* **2018**, *2018*, 228–247. [CrossRef]
6. Leong, W.L.; Vittal, J.J. One-Dimensional Coordination Polymers: Complexity and Diversity in Structures, Properties, and Applications. *Chem. Rev.* **2011**, *111*, 688–764. [CrossRef]
7. Marin, R.; Brunet, G.; Murugesu, M. Shining New Light on Multifunctional Lanthanide Single-Molecule Magnets. *Angew. Chem. Int. Ed.* **2021**, *60*, 1728–1746. [CrossRef]
8. Edelmann, F.T. Lanthanide Amidinates and Guanidinates in Catalysis and Materials Science: A Continuing Success Story. *Chem. Soc. Rev.* **2012**, *41*, 7657. [CrossRef]

9. Ferrando-Soria, J.; Pasán, J.; Ruiz-Pérez, C.; Journaux, Y.; Julve, M.; Lloret, F.; Cano, J.; Pardo, E. Spin Control in Oxamato-Based Manganese(II)-Copper(II) Coordination Polymers with Brick-Wall Layer Architectures. *Inorg. Chem.* **2011**, *50*, 8694–8696. [CrossRef]
10. Ferrando-Soria, J.; Grancha, T.; Julve, M.; Cano, J.; Lloret, F.; Journaux, Y.; Pasán, J.; Ruiz-Pérez, C.; Pardo, E. Ligand Effects on the Dimensionality of Oxamato-Bridged Mixed-Metal Open-Framework Magnets. *Chem. Commun.* **2012**, *48*, 3539. [CrossRef]
11. Grancha, T.; Acosta, A.; Cano, J.; Ferrando-Soria, J.; Seoane, B.; Gascon, J.; Pasán, J.; Armentano, D.; Pardo, E. Cation Exchange in Dynamic 3D Porous Magnets: Improvement of the Physical Properties. *Inorg. Chem.* **2015**, *54*, 10834–10840. [CrossRef]
12. Abhervé, A.; Grancha, T.; Ferrando-Soria, J.; Clemente-León, M.; Coronado, E.; Waerenborgh, J.C.; Lloret, F.; Pardo, E. Spin-Crossover Complex Encapsulation within a Magnetic Metal-Organic Framework. *Chem. Commun.* **2016**, *52*, 7360–7363. [CrossRef]
13. Fortea-Pérez, F.R.; Vallejo, J.; Julve, M.; Lloret, F.; De Munno, G.; Armentano, D.; Pardo, E. Slow Magnetic Relaxation in a Hydrogen-Bonded 2D Array of Mononuclear Dysprosium(III) Oxamates. *Inorg. Chem.* **2013**, *52*, 4777–4779. [CrossRef]
14. Vaz, R.C.A.; Esteves, I.O.; Oliveira, W.X.C.; Honorato, J.; Martins, F.T.; da Silva Júnior, E.N.; Valente, D.d.C.A.; Cardozo, T.M.; Horta, B.A.C.; Mariano, D.L.; et al. Lanthanide(III)-Oxamato Complexes Containing Nd^{3+} and Ho^{3+}: Crystal Structures, Magnetic Properties, and Ab Initio Calculations. *CrystEngComm* **2022**, *24*, 6628–6641. [CrossRef]
15. Vaz, R.C.A.; Esteves, I.O.; Oliveira, W.X.C.; Honorato, J.; Martins, F.T.; Marques, L.F.; Dos Santos, G.L.; Freire, R.O.; Jesus, L.T.; Pedroso, E.F.; et al. Mononuclear Lanthanide(III)-Oxamate Complexes as New Photoluminescent Field-Induced Single-Molecule Magnets: Solid-State Photophysical and Magnetic Properties. *Dalton Trans.* **2020**, *49*, 16106–16124. [CrossRef]
16. da Cunha, T.T.; Barbosa, V.M.M.; Oliveira, W.X.C.; Pinheiro, C.B.; Pedroso, E.F.; Nunes, W.C.; Pereira, C.L.M. Slow Magnetic Relaxation in Mononuclear Gadolinium(III) and Dysprosium(III) Oxamato Complexes. *Polyhedron* **2019**, *169*, 102–113. [CrossRef]
17. da Silveira, C.O.C.; Oliveira, W.X.C.; da Silva Júnior, E.N.; Alvarenga, M.E.; Martins, F.T.; Gatto, C.C.; Pinheiro, C.B.; Pedroso, E.F.; Silva, J.P.O.; Marques, L.F.; et al. Photoluminescence and Magnetic Properties of Isostructural Europium(III), Gadolinium(III) and Terbium(III) Oxamate-Based Coordination Polymers. *Dalton Trans.* **2024**, *53*, 14995–15009. [CrossRef]
18. Maciel, J.W.; de Souza, J.J.S.; Valdo, A.K.; Martins, F.T.; Guimarães, F.F.; de Santana, R.C.; Maia, L.J.Q.; Cangussu, D. Investigating Solid-State Luminescent Properties of New Cadmium(II) and Lead(II) Oxamato-Based Coordination Polymers. *J. Braz. Chem. Soc.* **2024**, *35*, e-20240072. [CrossRef]
19. De Oliveira Maciel, J.W.; Lemes, M.A.; Valdo, A.K.; Rabelo, R.; Martins, F.T.; Queiroz Maia, L.J.; De Santana, R.C.; Lloret, F.; Julve, M.; Cangussu, D. Europium(III), Terbium(III), and Gadolinium(III) Oxamato-Based Coordination Polymers: Visible Luminescence and Slow Magnetic Relaxation. *Inorg. Chem.* **2021**, *60*, 6176–6190. [CrossRef]
20. Maciel, J.W.; Kalinke, L.H.G.; Valdo, A.K.; Martins, F.T.; Rabelo, R.; Moliner, N.; Cano, J.; Julve, M.; Lloret, F.; Cangussu, D. New Metal-Organic Systems with a Functionalized Oxamate-Type Ligand and Mn^{II}, Fe^{II}, Cu^{II} and Zn^{II}. *J. Braz. Chem. Soc.* **2019**, *30*, 2413–2429. [CrossRef]
21. Oliveira, T.L.; Kalinke, L.H.G.; Mascarenhas, E.J.; Castro, R.; Martins, F.T.; Sabino, J.R.; Stumpf, H.O.; Ferrando, J.; Julve, M.; Lloret, F.; et al. Cobalt(II) and Copper(II) Assembling through a Functionalized Oxamate-Type Ligand. *Polyhedron* **2014**, *81*, 105–114. [CrossRef]
22. Sheldrick, G.M. Crystal Structure Refinement with SHELXL. *Acta Crystallogr. C Struct. Chem.* **2015**, *71*, 3–8. [CrossRef]
23. Spek, A.L. Single-Crystal Structure Validation with the Program PLATON. *J. Appl. Crystallogr.* **2003**, *36*, 7–13. [CrossRef]
24. Macrae, C.F.; Sovago, I.; Cottrell, S.J.; Galek, P.T.A.; McCabe, P.; Pidcock, E.; Platings, M.; Shields, G.P.; Stevens, J.S.; Towler, M.; et al. *Mercury 4.0*: From Visualization to Analysis, Design and Prediction. *J. Appl. Crystallogr.* **2020**, *53*, 226–235. [CrossRef]
25. Farrugia, L.J. *ORTEP-3*; School of Chemistry, University of Glasgow: Glasgow, Scotland, 2012.
26. Farrugia, L.J. WinGX and ORTEP for Windows: An Update. *J. Appl. Crystallogr.* **2012**, *45*, 849–854. [CrossRef]
27. Gruber, J.B.; Zandi, B.; Valiev, U.V.; Rakhimov, S.A. Energy Levels of $Dy^{3+}(^4f_9)$ in Orthoaluminate Crystals. *J. Appl. Phys.* **2003**, *94*, 1030–1034. [CrossRef]
28. Caspers, H.H.; Rast, H.E.; Fry, J.L. Absorption, Fluorescence, and Energy Levels of Ho^{3+} in LaF_3. *J. Chem. Phys.* **1970**, *53*, 3208–3216. [CrossRef]
29. Krupke, W.F.; Grdbee, J.B. Absorption and Fluorescence Spectra of $Er^{3+}(^4f_{11})$ in LaF_3. *J. Chem. Phys.* **1963**, *39*, 1024–1030. [CrossRef]
30. Rajnák, C.; Boča, R. Reciprocating Thermal Behavior in the Family of Single Ion Magnets. *Coord. Chem. Rev.* **2021**, *436*, 213808. [CrossRef]
31. Cole, K.S.; Cole, R.H. Dispersion and Absorption in Dielectrics I. Alternating Current Characteristics. *J. Chem. Phys.* **1941**, *9*, 341–351. [CrossRef]
32. Sahu, P.K.; Konar, S. Dysprosium (III) Based One-Dimensional Zigzag Chain Exhibiting Slow Magnetic Relaxation. *Inorganica Chim. Acta* **2024**, *572*, 122255. [CrossRef]
33. Orts-Arroyo, M.; Rabelo, R.; Carrasco-Berlanga, A.; Moliner, N.; Cano, J.; Julve, M.; Lloret, F.; De Munno, G.; Ruiz-García, R.; Mayans, J.; et al. Field-Induced Slow Magnetic Relaxation and Magnetocaloric Effects in an Oxalato-Bridged Gadolinium(III)-Based 2D MOF. *Dalton Trans.* **2021**, *50*, 3801–3805. [CrossRef] [PubMed]

34. El Alouani Dahmouni, N.; Orts-Arroyo, M.; Sanchis-Perucho, A.; Moliner, N.; Mayans, J.; Pacheco, M.; Castro, I.; De Munno, G.; Marino, N.; Ruiz-García, R.; et al. Magnetocaloric Efficiency Tuning through Solvent-Triggered 3D to 2D Interconversion in Holmium(III)-Based Dynamic MOFs. *Chem. Commun.* **2024**, *60*, 7451–7454. [CrossRef] [PubMed]
35. Daudin, B.; Lagnier, R.; Salce, B. Thermodynamic Properties of the Gadolinium Gallium Garnet, $Gd_3Ga_5O_{12}$, between 0.05 and 25 K. *J. Magn. Magn. Mater.* **1982**, *27*, 315–322. [CrossRef]
36. Numazawa, T.; Kamiya, K.; Okano, T.; Matsumoto, K. Magneto Caloric Effect in $(Dy_xGd+)_3Ga_5O_{12}$ for Adiabatic Demagnetization Refrigeration. *Physica B Condens. Matter* **2003**, *329–333*, 1656–1657. [CrossRef]
37. Saines, P.J.; Paddison, J.A.M.; Thygesen, P.M.M.; Tucker, M.G. Searching beyond Gd for Magnetocaloric Frameworks: Magnetic Properties and Interactions of the $Ln(HCO_2)_3$ Series. *Mater. Horiz.* **2015**, *2*, 528–535. [CrossRef]
38. Dixey, R.J.C.; Saines, P.J. Optimization of the Magnetocaloric Effect in Low Applied Magnetic Fields in $LnOHCO_3$ Frameworks. *Inorg. Chem.* **2018**, *57*, 12543–12551. [CrossRef]
39. Doheny, P.W.; Cassidy, S.J.; Saines, P.J. Investigations of the Magnetocaloric and Thermal Expansion Properties of the $Ln_3(Adipate)_{4.5}(DMF)_2$(Ln = Gd-Er) Framework Series. *Inorg. Chem.* **2022**, *61*, 4957–4964. [CrossRef] [PubMed]
40. Li, Z.; Arauzo, A.; Giner Planas, J.; Bartolomé, E. Magnetic Properties and Magnetocaloric Effect of Ln = Dy, Tb Carborane-Based Metal–Organic Frameworks. *Dalton Trans.* **2024**, *53*, 8969–8979. [CrossRef]
41. Li, Z.; Arauzo, A.; Roscini, C.; Planas, J.G.; Bartolomé, E. Multifunctional Self-Refrigerated Multivariate {GdLn} (Ln = Dy, Tb, Tb/Eu) Metal–Organic Frameworks. *J. Mater. Chem. A Mater.* **2024**, *12*, 21971–21986. [CrossRef]
42. Herrero, A.; Aseguinolaza, I.R.; Oleaga, A.; Garcia-Adeva, A.J.; Apiñaniz, E.; Garshev, A.V.; Yapaskurt, V.O.; Morozkin, A.V. Selecting Optimal R_6TX_2 Intermetallics (R = Gd, Tb, Dy; T = Mn, Fe, Co, Ni; X = Sb, Te) for Magnetic Refrigeration. *Dalton Trans.* **2023**, *52*, 5780–5797. [CrossRef]
43. Kleinhans, M.; Eibensteiner, K.; Leiner, J.C.; Resch, C.; Worch, L.; Wilde, M.A.; Spallek, J.; Regnat, A.; Pfleiderer, C. Magnetocaloric Properties of $R_3Ga_5O_{12}$ (R=Tb, Gd, Nd, Dy). *Phys. Rev. Appl.* **2023**, *19*, 014038. [CrossRef]

Disclaimer/Publisher's Note: The statements, opinions and data contained in all publications are solely those of the individual author(s) and contributor(s) and not of MDPI and/or the editor(s). MDPI and/or the editor(s) disclaim responsibility for any injury to people or property resulting from any ideas, methods, instructions or products referred to in the content.